ACS APPLIED MATERIALS & INTERFACES

www.acsami.org

Research Article

Two-Photon Polymerization of Bioinspired Microstructure with Tunable Wettability Controlled by Dielectric Elastomer Actuator

Zefu Ren,[#] Zhuoyuan Yang,[#] Rishikesh Srinivasaraghavan Govindarajan, Kehao Tang, Sida Xu, Meng Chen,* Yizhou Jiang,* and Daewon Kim*

Cite This: https://doi.org/10.1021/acsami.5c10911

Read Online

ACCESS | Metrics & More | Article Recommendations | Supporting Information

ABSTRACT: Bioinspired functional surfaces with tunable wettability have garnered significant attention in surface engineering due to their potential in applications, such as self-cleaning and microfluidic control. However, existing wettability modulation methods often face limitations in response time, control precision, and repeatability. Herein, this study presents a biomimetic design for active wettability control by integrating 3D-printed *Salvinia molesta*-inspired microstructures controlled by dielectric elastomer actuators (DEAs). Using two-photon polymerization, hierarchical eggbeater microstructures were precisely fabricated on a flexible, stretchable, and transparent polymer film, achieving robust interfacial bonding and demonstrating 90.8% shape recovery after deformation. Systematic evaluation of the hydrophobic properties revealed that designs with a higher number of concentric rings and reduced center-to-center spacing exhibited enhanced water droplet adhesion while maintaining Cassie−Baxter state suspension. The fabricated microstructures demonstrated tunable hydrophobicity, achieving contact angles of 140.8 ± 1.4° to 149.7 ± 1.8° in the Cassie−Baxter state and roll-off angles of 5.7 ± 0.9° to 30.0 ± 1.6°, indicating precise control over wetting behavior. The DEA system enabled dynamic wettability modulation through voltage-controlled adjustment of microstructure spacing, facilitating rapid transitions from Cassie−Baxter to Wenzel states. In addition, the DEA-induced programmable microstructure enabled surface adhesion modification, allowing droplet manipulation and transportation. This innovative integration of biomimetic microstructures with DEA technology offers significant potential for advanced applications requiring fast, reversible wettability control, including droplet-based microfluidics and active self-cleaning surfaces.

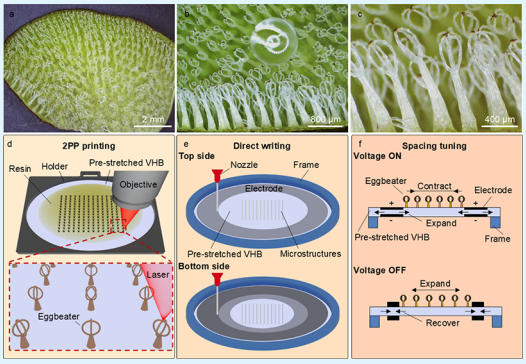

KEYWORDS: *bioinspired microstructures, two-photon polymerization, Ccontrollable wettability, droplet transportation, DEA, additive manufacturing*

1. INTRODUCTION

Natural hydrophobic surfaces, such as those found on lotus leaves, rose petals, and *Salvinia molesta* (*S. molesta* hereafter), exhibit remarkable functional properties, including self-cleaning, microfluidic manipulation, and anti-icing capabilities.[1−4] Particularly, *S. molesta* stands out for its superhydrophobicity, high water contact angle (CA), long-term air retention underwater, and low-friction fluid transport.[5,6] The unique eggbeater structure on the leaf surface consists of a stalk and a crown-like head with four connected branches. *S. molesta* surfaces achieve their superhydrophobic performance through hierarchical structures with a nanoscopic wax crystal layer that creates Cassie−Baxter wetting, forming a near-spherical droplet suspended on the surface.[7] Air pockets are trapped beneath water droplets, minimizing the liquid−solid interface and enhancing the liquid−air interface.[8] On the other hand, a water droplet that fully penetrates surface structures is in the Wenzel state, resulting in lower contact angles with strong adhesion.[9]

Replicating such a complex eggbeater structure of *S. molesta* is essential for reproducing its exceptional superhydrophobic properties, which require high-resolution spatial fabrication. Recent advances in high-resolution 3D printing, particularly ultraviolet (UV)-based photopolymerization, have enabled accurate biomimicry of these complex structures.[10−13] For instance, a 1:1 scale reproduction of *S. Molesta*-inspired microstructures was successfully achieved using a projector-based UV 3D printer with a resolution of 2.5 μm.[14] The printed structure demonstrated superhydrophobic (CA: 152°−170°) and the ability to hold the water droplet upside down, known as the Petal effect. For applications in microfluidics and other miniaturized systems, the fabrication of reduced-scale

Received: June 3, 2025
Revised: October 17, 2025
Accepted: October 26, 2025

structures becomes particularly advantageous. This need has driven the adoption of two-photon polymerization (2PP), capable of micro- and submicroscale fabrication. This process relies on simultaneous two-photon absorption in photosensitive resin, where polymerization initiates only when the laser's focal point exceeds a material-specific energy threshold.[15−17] Ellipsoidal voxels (typically 100−400 nm in size) are periodically arranged along the laser path to build a microstructure.[18−20] Remarkably, eggbeater structures were successfully fabricated at 17.5× and 100× reduced scales while maintaining the functionalities of natural *S. molesta*, including underwater air retention and hydrophobicity demonstrated by CA of 170° with Teflon coating and 122° without modification.[21,22]

In recent years, microstructured surfaces exhibited fixed wettability characteristics and demonstrated superior mechanical robustness, thermal stability, and chemical resistance.[23−28] With the development of responsive systems incorporating thermal, magnetic, and electrowetting-on-dielectric (EWOD) actuation mechanisms,[29−37] dynamically tunable wettability patterns are achieved. Thermal-responsive wetting surfaces were typically fabricated from thermosensitive materials such as shape memory polymers or waxes.[38−41] While they can reversibly change surface wettability, their response rate is inherently limited because heating and cooling processes are relatively slow. In contrast, magnetic-responsive exhibited fast response and excellent stability. Microstructures infused with magnetic particles could be reconfigured by an external magnetic field to manipulate droplets.[42−45] However, the presence of a magnetic field gradient resulted in spatially nonuniform wettability changes, which may reduce control precision across the surface. EWOD provides highly precise, localized control of droplet motion by electrically modulating the solid−liquid contact angle.[46−48] By applying voltage to patterned electrodes beneath a dielectric layer, droplets on the dielectric layer could be transported, merged, split, or steered along predefined pathways. However, the intense electric field generated by the applied voltage at the droplet interface may induce secondary droplet formation, which can disrupt transport accuracy.[37] In contrast, dielectric elastomer actuators (DEAs) overcome these limitations by offering millisecond-scale responsiveness, high repeatability, and voltage-driven programmability, making them ideal for on-demand wettability switching.[49,50] A DEA consists of a soft dielectric elastomer layer sandwiched between two compliant electrodes. When voltage is applied across the electrode layers, Maxwell stress is induced, leading to a reduction in the dielectric thickness and a corresponding in-plane expansion of the actuator.[51] This electromechanical actuation results in rapid and reversible surface deformation, allowing dynamic modulation of microstructural geometry for controllable wettability. To achieve optimal electromechanical performance, the dielectric materials need to exhibit low moduli, high electrical breakdown strength, and high dielectric constant.[52] Acrylic elastomers, such as VHB 4910 and VHB 4905 (3M, Minnesota, USA), have become common materials due to their commercial availability, low cost, and exceptional stretchability. In addition, these elastomers are typically prestretched to reduce the thickness before electrode deposition, which allows DEAs to lower operational voltages and mitigate the electromechanical instability.[53,54] Moreover, the compliant electrodes, such as carbon grease, liquid metal, and Poly(3,4-ethylenedioxythiophene):poly(styrenesulfonic acid) (PEDOT:PSS), exhibit high conductivity and are feasible for 3D printing.[55−57] Among these electrode materials, carbon grease-based electrode ink offers distinct advantages, including environmental stability and exceptional crack tolerance for high-strain applications.[58]

This study introduces a novel planar DEA integrated with 3D-printed *S. molesta*-inspired microstructures, capable of rapidly adjusting surface wettability in response to electrical stimuli. The fabrication process employed optimized 2PP to precisely replicate bioinspired eggbeater microstructures on a flexible, stretchable, and transparent VHB film substrate while ensuring robust interfacial bonding for enhanced durability. The hydrophobic properties of these microstructures were systematically characterized through water CA and roll-off angle (RA) measurements across various crown designs and spacing configurations. For electromechanical control, carbon grease-based compliant electrodes were patterned onto the VHB film using direct writing (DW) techniques, enabling voltage-dependent adjustment of microstructure spacing for on-demand wettability tuning. A comparison of our work with existing literature is shown in Supporting Information Table S1. This innovative integration of biomimetic microstructures with DEA technology offers significant potential for advanced applications in droplet-based active droplet transportation and manipulation, where fast, reversible wettability control is essential.

2. EXPERIMENTAL SECTION

2.1. Eggbeater Microstructure and DEA Fabrication. The eggbeater microstructures were fabricated using a Nanoscribe GT2 printer (Eggenstein-Leopoldshafen, Germany), which operates with a 780 nm laser featuring a pulse duration of 100 fs and a repetition rate of 80 MHz. The computer-aided design model of the *S. molesta*-inspired microstructure was processed using DeScribe software with default printing parameters for the 25× objective lens and IP-S photoresist (Nanoscribe, Eggenstein-Leopoldshafen, Germany). The slicing and hatching distances were set to 1 and 0.5 μm, respectively.

To prepare for the 2PP process, a VHB 4905 film (50 mm in diameter and 0.5 mm in thickness) was stretched to three times its original diameter, and the thickness was measured to be 52.8 ± 1.3 μm (Supporting Information Figure S1). The prestretched VHB was then secured onto the substrate holder of a 2PP printer using polyimide tape. A drop of IP-S photoresist was deposited at the center of the prestretched VHB. After installing a cleaned 25× objective lens in the printer (Nanoscribe, Eggenstein-Leopoldshafen, Germany), the substrate holder was positioned above the objective lens. Five base layers were printed on the interface at 80% laser power (a maximum power of 50 mW) with a scanning speed of 100 mm/s. Subsequently, the laser power was increased to 95% to fabricate the remaining layer. These laser powers were adjusted to avoid overexposure while maintaining structural integrity. The VHB substrate with fabricated microstructures was removed from the printer and developed in isopropanol (IPA) for 5 min to dissolve any uncured excess photosensitive resin (Supporting Information Figure S2).

Following the 2PP printing process, the DEA was fabricated by depositing electrode material on the patterned VHB film using a DW 3D printer (5552202-Dispensing Robot, Integrated Dispensing Solutions, USA). The electrode material consisted of 97 wt % carbon conductive grease (MG

https://doi.org/10.1021/acsami.5c10911
ACS Appl. Mater. Interfaces XXXX, XXX, XXX−XXX

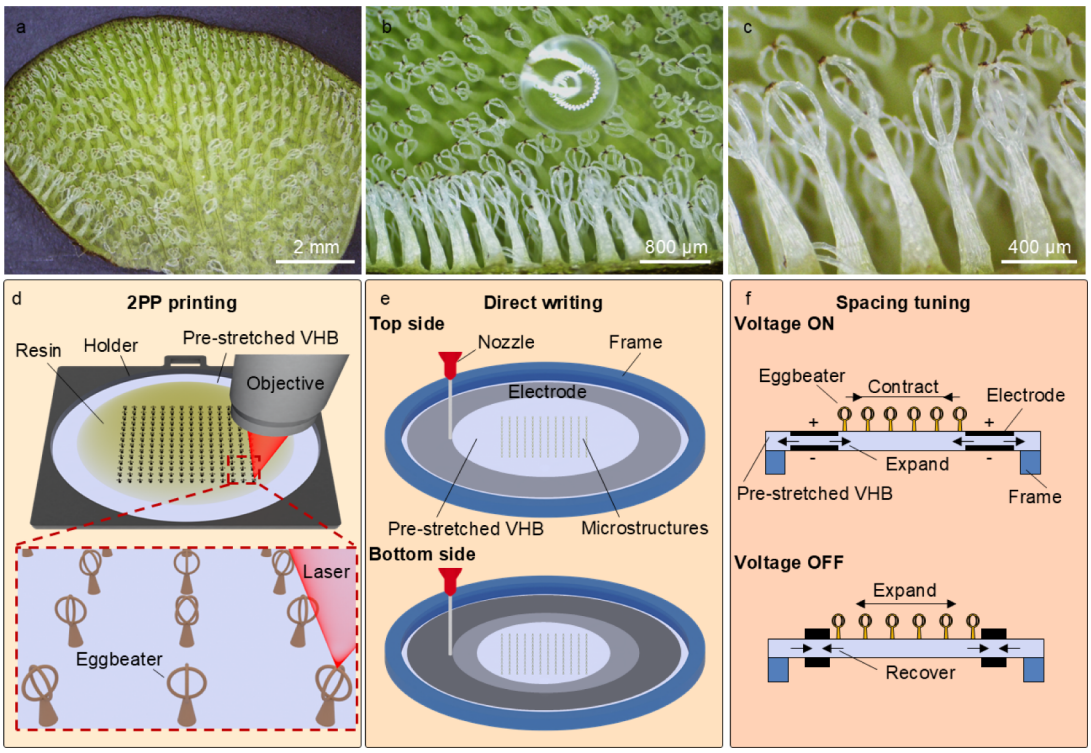

Figure 1. Design, manufacturing, and actuation of bioinspired DEA with tunable spacing. (a) Optical image of a natural *S. molesta* leaf. (b) A droplet was suspended on superhydrophobic eggbeater microstructures. (c) Detailed view of eggbeater hairs. (d) 2PP printing process for fabricating biomimetic microstructures on prestretched VHB substrate. (e) DEA assembly with compliant electrodes by direct writing. (f) Voltage-induced tunable spacing mechanism.

Chemicals, Canada) and 3 wt % carbon black (Timical Super C65, MTIKorea, Korea), mixed using a THINKY ARM-310 planetary mixer (Laguna Hills, CA, USA) at 2000 rpm for 2 min. The mixture demonstrated DW printing capability and excellent conductivity for DEA application (Supporting Information Figures S3 and S4). The electrode material was loaded into a 30 mL syringe with a 19-gauge nozzle. It was then patterned using DW, with the printed line width set to 0.55 mm and the initial nozzle height set to 0.2 mm. The air pressure was maintained at 0.5 MPa, and the nozzle was moved at a speed of 2 mm/s during printing.

2.2. Scanning Electron Microscopy. The printed microstructures were examined using an FEI Quanta 650 scanning electron microscope (SEM). Before imaging, a thin gold coating was applied to the samples with a 108 Manual sputter coater (Ted Pella, Redding, USA).

2.3. Normal Bonding Strength, Shear Bonding Strength, and Flexibility Evaluation. Bonding strength was evaluated to ensure reliable microstructure integration. A layer of IP-S resin (500 μm in thickness) was coated on both sides of the prestretched VHB substrate (2.5 cm × 2.5 cm, 50 μm in thickness), which was then sandwiched between transparent acrylic plates. The samples were exposed to 400 W UV light for 60 s. The normal and shear bonding strengths between the cured IP-S resin and the prestretched VHB film were evaluated under normal tensile test and lap shear test, respectively, using a universal test machine MTS C43.504 (MTS Systems Corporation, USA) at a rate of 0.2 mm/min. The adhesive strength was calculated by dividing the maximum sustained load by the VHB contact area. The durability of the printed microstructure on the VHB substrate was evaluated by the tilt recovery test. The printed microstructure on the VHB film was tilted to touch the base. The corresponding level of retraction was observed under the digital microscope VHX-X1 (Keyence, Japan).

2.4. Water Contact Angle and Roll-Off Angle Measurement. The water CA measurements were performed 5 times for each sample using a digital microscope VHX-X1 (Keyence, Japan) under controlled ambient conditions (23.5 ± 0.5 °C, 50 ± 2% relative humidity). Different volumes of deionized (DI) water droplets ranging from 8 to 80 μL were tested, and the result indicated a limited influence on wettability (Supporting Information Figure S5). A water droplet was deposited onto the microstructures with a micropipette, and the CA was determined using ImageJ software. A custom-made VHB film holder was fixed to the rotational stage, which was securely mounted vertically on a flat wall surface. The VHB film containing the printed microstructures was then placed horizontally on the holder, ensuring that the center of the microstructures aligned with the stage's rotation axis. A water droplet was deposited onto the microstructure, and the RA was recorded when the droplet slid off as the stage rotated.

2.5. Characterization of DEA Controllability and Durability. The dielectric strength of the prestretched VHB films was measured with a high-voltage amplifier, TREK 20/20C-HS (Denver, CO, USA), and a dielectric breakdown test system, PK-CPE1901 (PolyK Technologies, LLC, PA, USA), according to ASTM D149.59. The applied voltage was increased by 200 V/s until breakdown occurred. The deformation of the DEA was measured using a VHX-X1 digital microscope while the voltage gradually increased from 0 V to its maximum voltage before breakdown with an increment of 200 V. The response time of the DEA was examined at 3 kV

https://doi.org/10.1021/acsami.5c10911
ACS Appl. Mater. Interfaces XXXX, XXX, XXX−XXX

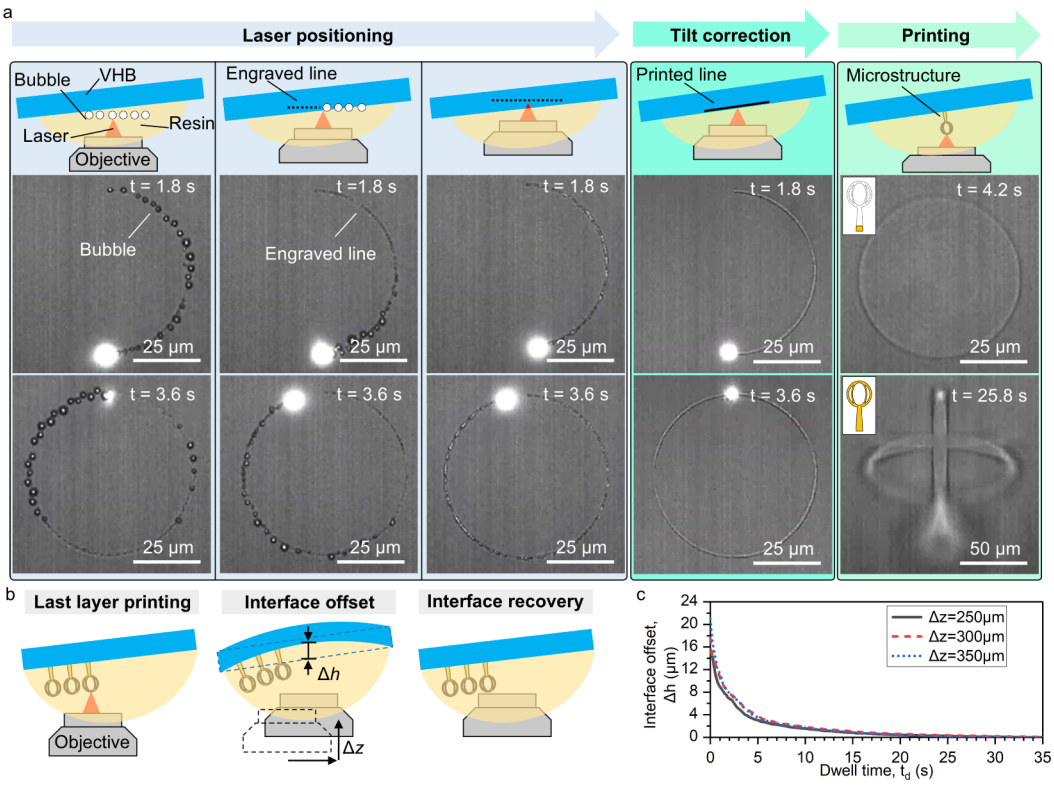

Figure 2. (a) Interface finding process on a tilted transparent VHB substrate for 2PP printing. (b) Schematic of the deflected flexible substrate's recovery process while the objective moves. (c) Representative curves of interface offset vs dwell time at various objective vertical movements.

(below breakdown voltage) from 1 s to 50 ms (Supporting Information Video S1). In addition, the durability of DEA was examined by conducting long-term cycling tests at 6 Hz and 3 kV (Supporting Information Video S2).

3. RESULTS AND DISCUSSION

3.1. Design and Fabrication of Eggbeater Microstructures. To develop compact artificial structures mimicking *S. molesta*'s hydrophobic functionality, its natural morphology was observed through microscopic imaging. The upper surface of the leaf was covered by millimetric hierarchical hairs (Figure 1a). The dense arrangement of these structures creates a superhydrophobic surface that suspends a water droplet while maintaining spherical shape (Figure 1b,c). Notably, the water droplet made direct contact with the crown structures, demonstrating its dominant role in maintaining surface hydrophobicity. To balance fabrication efficiency with wettability performance, these synthetic structures were designed about 5× smaller compared to their natural counterparts (Supporting Information Figure S6). The artificial hair consisted of a 100 μm-high taper-shaped stalk, featuring a base diameter of 50 μm for robust substrate adhesion and a 30 μm tip diameter for a smooth transition to the upper structure. The crown structures were composed of multiple concentric torus, having 50 μm major and 10 μm minor radii, arranged with uniform angular distribution (Supporting Information Figure S7). The 2PP fabrication process employed a 25× objective immersed in IP-S resin deposited on a prestretched VHB 4905 substrate firmly adhered to the substrate holder. Through laser-induced polymerization, precise biomimetic microstructure arrays were created (Figure 1d). Following development and transfer to a circular frame, the DEA was completed by pneumatically depositing compliant carbon grease electrodes on both surfaces of the prestretched VHB film (Figure 1e). When voltage is applied, Maxwell stress is generated between the compliant electrodes, causing the VHB dielectric layer to be compressed in thickness while being expanded in-plane. This deformation results in reduced spacing between adjacent microstructures. Upon voltage removal, the original dimensions of the VHB elastomer are elastically recovered, with the microstructure spacing being fully restored (Figure 1f).

While the DEA enabled microstructure spacing adjustment, precise fabrication of these microstructures via 2PP first required solving a critical interfacial challenge. Unlike printing on rigid substrates, the compliant nature and optical transparency of prestretched VHB films created significant difficulties in locating the resin-substrate interface during 2PP printing. This positioning uncertainty risked producing either floating microstructures (if printed above the substrate) or incomplete structures (if printed too deep within the substrate). The resin-substrate interface could be automatically identified by the GT2 printer when a minimum reflectance existed near the focal plane of the 25× objective. Since the refractive indices of IP-S resin and VHB film were 1.486 and 1.483, respectively,[60,61] resulting in a reflectance of approximately 1×10^{-6} based on the Fresnel reflection coefficient at normal incidence,[62] manual interface detection is required. As illustrated in Figure 2a, after the objective reached the air–liquid interface, a laser was activated and scanned at a speed of 0.1 mm/s with 80% laser power along a horizontal circular path to polymerize the IP-S resin. Compared to normal printing speed, the relatively low scanning speed was chosen because it generated bubbles in IP-S resin at the laser focal point. However, when the laser focal point reached the resin-VHB interface, a partial circular pattern composed of an

https://doi.org/10.1021/acsami.5c10911
ACS Appl. Mater. Interfaces XXXX, XXX, XXX−XXX

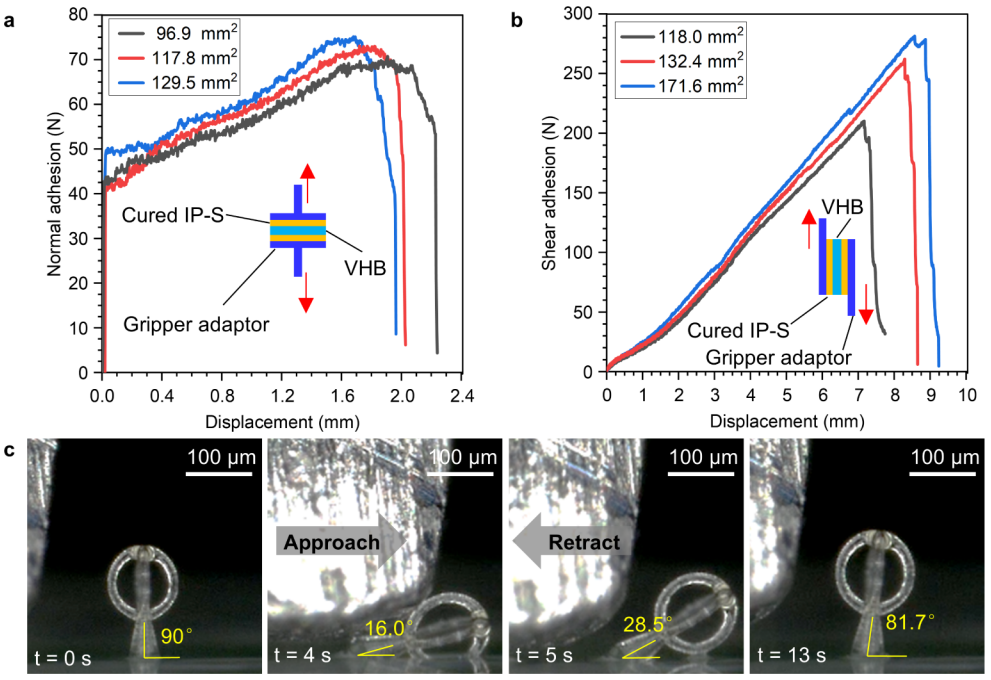

Figure 3. (a) Representative force−displacement curves of the normal adhesion test. (b) Representative force−displacement curves of the lap shear test. (c) Tilt recovery test of a printed microstructure.

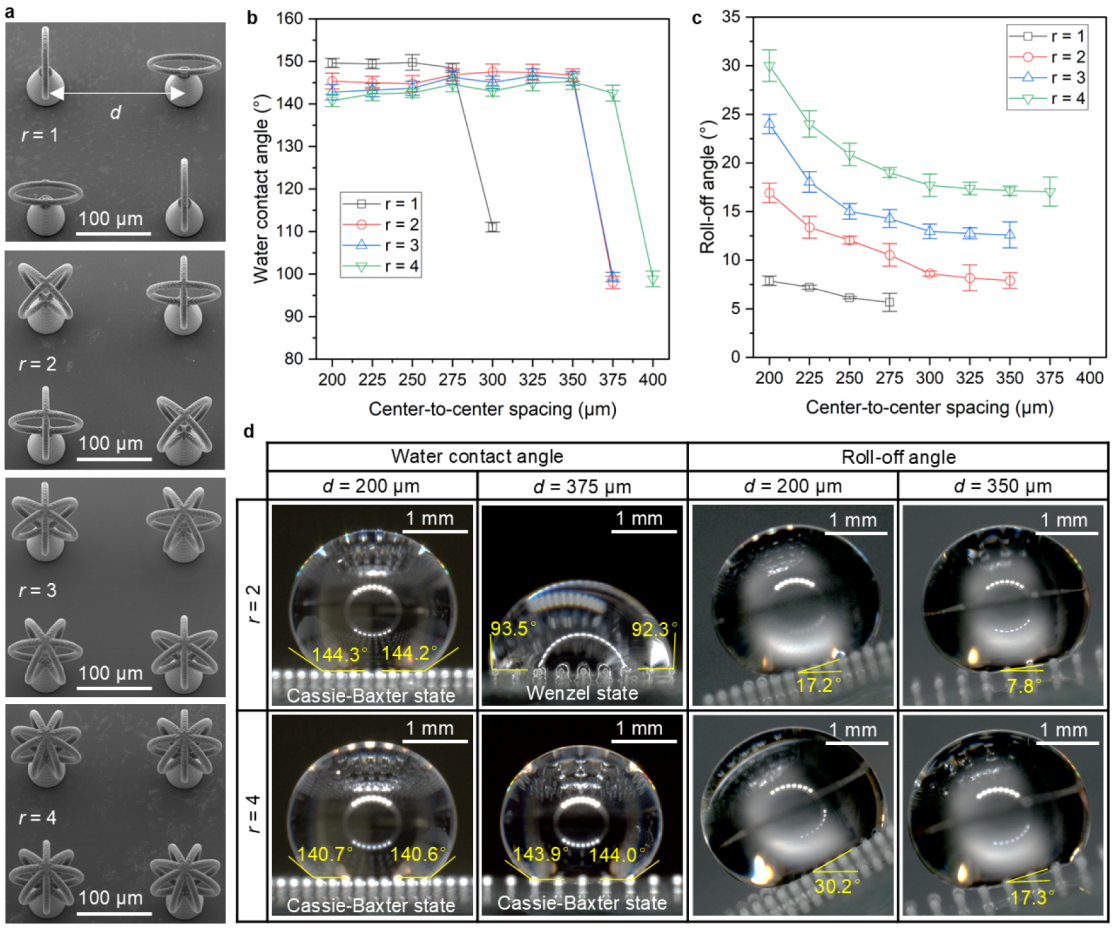

Figure 4. Wettability performance of *S. molesta* inspired crown-like microstructures. (a) SEM image of fabricated microstructures with various numbers of concentric rings. (b) Water CA versus center-to-center spacing for all ring configurations. (c) RA versus center-to-center spacing for all configurations, maintaining Cassie−Baxter state. (d) Representative droplet profiles during water CA and RA tests, droplet size: 8.0 μL.

https://doi.org/10.1021/acsami.5c10911
ACS Appl. Mater. Interfaces XXXX, XXX, XXX−XXX

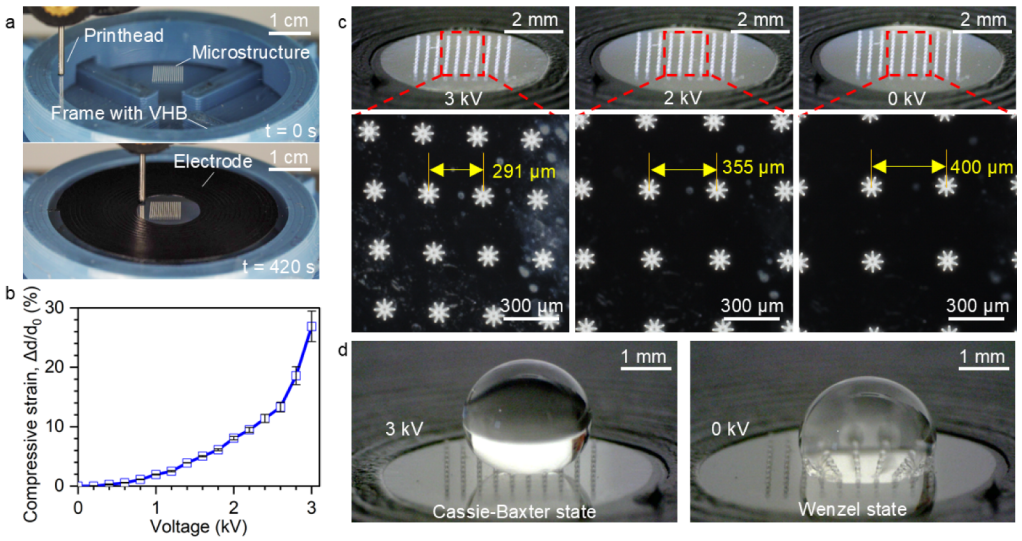

Figure 5. Fabrication and electromechanical characterization of the DEA. (a) DW process for electrode patterning. (b) Voltage-dependent compressive strain at the center-to-center spacing of the eggbeater microstructures. (c) Tunable center-to-center spacing during voltage release (d) Wettability transition from Cassie−Baxter to Wenzel states via voltage control, droplet size: 8.0 μL.

engraved line and bubbles was formed on the nonlevel substrate. Once a complete circular line was engraved, the solid interface was found, and the XYZ coordinates of the center were recorded for tilt correction (Supporting Information eqs S1−S4). By repeating this laser positioning method to obtain three different coordinates, the rotation angles between the substrate and the XY-plane were calculated. The circular path was then corrected using the computed rotation angles, and the final interface was determined. Finally, the microstructure was successfully printed and firmly adhered to the VHB substrate.

After completing one microstructure fabrication, the objective moved to a new starting position (Figure 2b). However, due to the stretchable nature of VHB film, high viscous properties of IP-S resin, and the objective vertical displacement (Δz), the substrate-resin interface experienced vertical shifting, resulting in interface offset (Δh). Following a dwell time (t_d), the VHB film gradually returned to its original position, allowing the laser focal point to realign with the interface. Experimental results indicated that a 25-s t_d provided over 99.5% offset recovery (Figure 2c), balancing print efficiency and quality across various Δz values caused by microstructure height and substrate tilt.

3.2. Mechanical Performance of Eggbeater Microstructure on VHB Substrate. To ensure the durability of the printed microstructure on the VHB substrate, the interfacial adhesion between polymerized IP-S resin and the VHB film was evaluated. Both normal adhesion and lap shear tests were performed (Figure 3a,b). Distinct failure modes were observed: the normal test exhibited adhesive failure at the interface, while the shear test showed cohesive failure within the VHB layer. The calculated normal and shear bonding strengths reached 0.6 ± 0.1 MPa (normal) and 1.8 ± 0.2 MPa (shear).

To verify the microstructure's ability to retain its designed configuration under external lateral forces, tilt recovery experiments were conducted (Figure 3c). An eggbeater microstructure was displaced to 16.0°, and it adhered to the VHB substrate. During this process, the substrate bonded to the stem structure's base exhibited significant stretching. Upon load removal, the stretched VHB film elastically contracted, restoring the microstructure to its original position with 90.8% recovery. Notably, the adhesive force generated between the crown structure and the VHB substrate remained below the bonding established at the eggbeater's root during 3D printing, enabling shape recovery after full tilting deformation. In addition, the eggbeater microstructure demonstrated 87.4% shape recovery after continuous 10,000 cycles of VHB actuation (Supporting Information Figure S8), with only a 3.4% decrease in recoverability.

3.3. Evaluation of Eggbeater Microstructure Surfaces' Wettability. Since the crown architecture governs the wetting performance of *S. molesta*'s eggbeater hairs, strategic modifications to its geometry, including the number of concentric rings (r) and center-to-center spacing distances (d), enable precise wettability tuning for targeted applications. Drawing inspiration from the natural morphology of *S. molesta*, four distinct crown-like architectures were developed by varying the number of r, ranging from 1 to 4, with uniform radial distribution (Figure 4a). In addition, multiple d values were incorporated into the designs to investigate wettability modification. Each adjacent microstructure was rotationally offset by 90°/r along its vertical axis, mitigating anisotropic wetting effects that were particularly crucial for designs with fewer rings.

The CA and RA were measured for all the designs with varying r, with representative cases of r = 2 and r = 4 (Figure 4b-d). The r = 2 configuration was selected to mimic the natural morphology of *S. molesta*, while r = 4 was chosen to provide a controlled comparison at twice the natural ring number. For all configurations, CA measurement was initiated at d = 200 μm, progressively increasing in 25 μm increments until an abrupt CA reduction indicating the wetting state transition from Cassie−Baxter to Wenzel state (Figure 4b). All ring designs exhibited hydrophobicity (140.8 ± 1.4° − 149.7 ± 1.8°) in Cassie−Baxter mode, transitioning to Wenzel mode with reduced CA (98.1 ± 1.5° − 111.0 ± 1.1°) when structural support failed. The critical d required to trigger wetting state transitions exhibited a positive correlation with r. Specifically, higher r values necessitated larger d thresholds to induce the

https://doi.org/10.1021/acsami.5c10911
ACS Appl. Mater. Interfaces XXXX, XXX, XXX−XXX

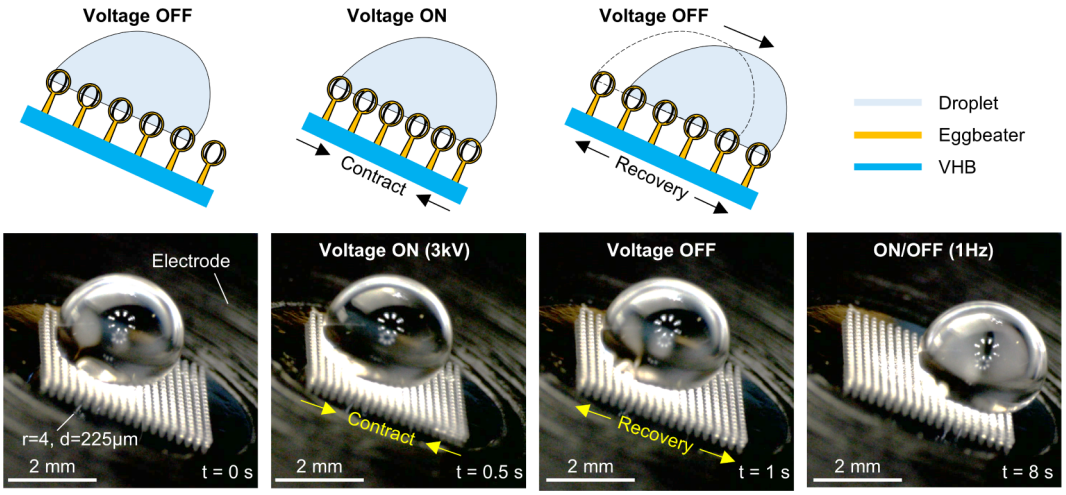

Figure 6. Schematic and demonstration of precise droplet manipulation by cyclically actuated DEA with microstructure arrays (r = 4, d = 225 μm) with 20° inclination, droplet size: 8.0 μL.

Cassie-to-Wenzel transition. While in the Cassie−Baxter wetting state, designs with lower r values demonstrated enhanced hydrophobic performance, consistent with previous studies.[14,22] This correlation was explained by the enhanced solid−liquid interfacial contact resulting from increased accessible surface area at higher r values. As the water droplet was subjected to a more microstructural surface area, the consequent reduction of the air−liquid interface directly decreases the CA. In contrast, no correlation was observed between spacing and CA in the Cassie−Baxter state.

In addition, the RA was subsequently measured exclusively for designs maintaining Cassie−Baxter wetting state (Figure 4c). The RA analysis revealed that both designs with higher r values and those with smaller d spacing exhibited increased RA ($5.7 \pm 0.9° - 30.0 \pm 1.6°$). This observation can be explained by the elevated solid−liquid interfacial density per unit area, which enhances water droplet adhesion to the microstructural arrays.[22]

3.4. Functional Performance of DEA-Actuated Wettability. The prestretched VHB film containing 4 mm × 4 mm microstructure arrays was mounted on a custom frame. A DEA was then produced by patterning electrodes on both VHB surfaces via DW. The deposited concentric conductive rings (20 mm outer and 8 mm inner diameters) were designed to prevent contact between the printhead, holder rim, and central microstructures, as shown in Figure 5a. The prestretched VHB breakdown at 3.2 kV, resulting in 64 V/μm breakdown strength. When voltage was applied, the generated electric field across the prestretched VHB caused electrostatic attraction between the opposing conductive layers. This Maxwell stress induced radial compression of the elastomer film, simultaneously producing two counteracting effects. While the conductive ring's outer perimeter expanded outward due to the elastomer's incompressible nature, its inner diameter contracted as the prestretch deformation partially recovered. The deformation of DEA from 0 to 3 kV was simulated based on the hyperelastic model in ANSYS (Supporting Information Figure S9 and eqs S5−S8). In addition, the strain in the center-to-center distance of the eggbeater microstructures was measured under applied voltages from 0 to 3 kV in 0.2 kV increments (Figure 5b). The measured strain exhibited nonlinear, accelerated progression with increasing voltage, reaching 28% maximum compression at 3 kV before dielectric breakdown. The reversible contraction of the microstructure array was observed (Figure 5c) as the voltage was decreased from 3 kV to 0 kV, with a corresponding increase in center-to-center spacing being illustrated. Additionally, the crown structures retained their original geometry when the VHB substrate was deformed. To demonstrate wettability modulation, a 3 kV voltage was applied to a DEA incorporating an r = 4 microstructure array with 400 μm center-to-center spacing. Initially, the deposited droplet was supported by the contracted microstructures in the Cassie−Baxter state (3 kV). Subsequently, the transition to the Wenzel state occurred as the spacing increased (0 kV). This bioinspired wettability tuning process was achieved through electrically controlled center-to-center spacing adjustment using DEA (Supporting Information Video S3).

The spacing of the microstructures was modulated to achieve precise droplet displacement, as shown in Figure 6 and Supporting Information Video S4. A DI water droplet was placed on a DEA-actuated bioinspired microstructure array (r = 4, d = 225 μm) and was tilted to 20° slightly below the roll-off threshold. Due to gravity, the advancing angle of the droplet increased, and the receding angle decreased as the tilt angle increased. Upon voltage application, the spacing between microstructures was reduced, causing the lower edge of the droplet to come into contact with the neighboring eggbeater microstructures. The reduced spacing increased the overall RA of the surface, allowing the droplet to remain securely pinned in place while maintaining the Cassie−Baxter state. When the voltage was removed, the lower edge of the droplet advanced with the newly contacted microstructure, while the upper edge detached from the previous one. By applying 1 Hz and 3 kV, continuous and precise droplet displacement was achieved, with resolution determined by the design of the microstructure array.

To demonstrate tunable hydrophobic properties, a DEA-actuated bioinspired microstructure array (r = 4, d = 225 μm) was inverted and mounted on an XYZ positioner, placing it above a DI water droplet resting on the left base microstructure array (r = 1, d = 275 μm), as shown in Figure 7. The design of the base microstructure arrays was selected to create a hydrophobic surface with low droplet adhesion. Not only the selected design on the voltage-activated DEA was required to generate sufficient adhesion force to overcome both the

https://doi.org/10.1021/acsami.5c10911
ACS Appl. Mater. Interfaces XXXX, XXX, XXX−XXX

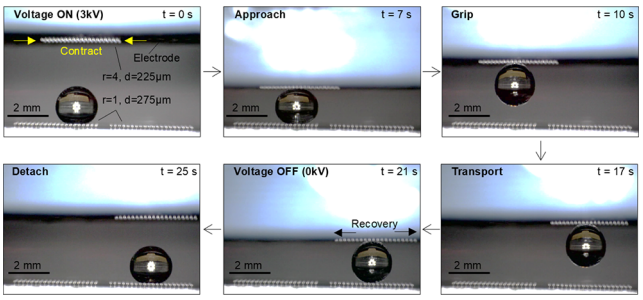

Figure 7. Tunable droplet gripper via bioinspired microstructure arrays. Two microstructure arrays (r = 1, d = 275 μm) on a base substrate with a 5.0 μL water droplet deposited on the left, and a DEA-controlled microstructure array (r = 4, d = 225 μm) on the top.

droplet's weight and the base microstructures' adhesion but also guaranteed reliable droplet release upon DEA deactivation. Upon voltage application, the microstructure arrays contracted to enhance droplet adhesion, and then the system successfully gripped and transported the water droplet. During deposition on the right base microstructure array (r = 1, d = 275 μm), voltage deactivation reduced the adhesion, enabling droplet release upon retraction, showcasing a successful water droplet manipulation utilizing novel tunable DEA with bioinspired structures. This actively controlled system demonstrates significant potential for liquid gripping (Supporting Information Video S5).[59]

4. CONCLUSIONS

This study established a novel approach integrating *S. molesta*-inspired microstructure fabrication and electromechanically tunable wettability control. Bioinspired microstructures were successfully fabricated on a prestretched VHB film (flexible, stretchable, and transparent) through 2PP using a laser positioning method with balanced printing efficiency and quality. The fabricated microstructures demonstrated excellent bonding with the VHB substrate and exhibited 90.8% shape recovery after deformation. The hydrophobic properties of the printed microstructure arrays were systematically evaluated through water CA (140.8 ± 1.4° − 149.7 ± 1.8°) and RA (5.7 ± 0.9° − 30.0 ± 1.6°) measurements across varying ring numbers and center-to-center spacing. Microstructure arrays with higher ring numbers and reduced spacing exhibited enhanced water droplet adhesion while maintaining the Cassie−Baxter state, leading to lower water CA and higher roll-off angle. Programmable droplet manipulation was achieved by integrating the microstructure arrays into the DEA system, which offers fast response, precise control, and exceptional repeatability. It enabled voltage-induced wetting state transitions (Cassie−Baxter to Wenzel) and controlled droplet transportation. The developed 2PP-printed bioinspired surfaces combined with DEA actuation offer significant potential for applications in tunable surface wetting, microfluidic transport, and self-cleaning surfaces. Future research directions include developing multi-DEA systems for localized wettability control and expanding the functional bioinspired area by directly fabricating microstructures on stretchable conductive electrodes.

ASSOCIATED CONTENT

Supporting Information

The Supporting Information is available free of charge at https://pubs.acs.org/doi/10.1021/acsami.5c10911.

VHB stretching device; eggbeater microstructures development duration; electrode ink's viscosity and moduli; electrode ink's conductivity; effect of droplet size on microstructure; effect of eggbeater scaling ratio on wettability; tilt recovery test of a printed microstructure after cyclic test; simulation of DEA deformation (PDF)

DEA response time ranges from 1 s to 50 ms (MP4)

Cyclic actuation test of the DEA conducted for 10,000 cycles (MP4)

Wetting state transition from Cassie−Baxter to Wenzel state using a DEA (MP4)

Droplet manipulation system with precise control on an inclined surface (MP4)

Tunable droplet gripper via DEA and bioinspired microstructure arrays (MP4)

AUTHOR INFORMATION

Corresponding Authors

Meng Chen − *Key Laboratory of Metallurgical Equipment and Control Technology, Ministry of Education, Wuhan University of Science and Technology, Wuhan, Hubei 430081, China*; Email: chengmeng@wust.edu.cn

Yizhou Jiang − *Department of Aerospace Engineering, Embry-Riddle Aeronautical University, Daytona Beach, Florida 32114, United States*; orcid.org/0009-0009-4802-8217; Email: yizhou.jiang@erau.edu

Daewon Kim − *Department of Aerospace Engineering, Embry-Riddle Aeronautical University, Daytona Beach, Florida 32114, United States*; orcid.org/0000-0003-3885-3925; Email: kimd3c@erau.edu

Authors

Zefu Ren − *Department of Aerospace Engineering, Embry-Riddle Aeronautical University, Daytona Beach, Florida 32114, United States*

Zhuoyuan Yang − *Department of Aerospace Engineering, Embry-Riddle Aeronautical University, Daytona Beach, Florida 32114, United States*

Rishikesh Srinivasaraghavan Govindarajan − *Department of Aerospace Engineering, Embry-Riddle Aeronautical University, Daytona Beach, Florida 32114, United States; Department of Mechanical Engineering, Florida Polytechnic University, Lakeland, Florida 33805, United States*

Kehao Tang − *Key Laboratory of Metallurgical Equipment and Control Technology, Ministry of Education, Wuhan University of Science and Technology, Wuhan, Hubei 430081, China*

Sida Xu − *Department of Aerospace Engineering, Embry-Riddle Aeronautical University, Daytona Beach, Florida 32114, United States*

Complete contact information is available at: https://pubs.acs.org/10.1021/acsami.5c10911

Author Contributions

#Z.R. and Z.Y. contributed equally to this work. The manuscript was written through contributions from all authors. All authors have approved the final version of the manuscript.

https://doi.org/10.1021/acsami.5c10911
ACS Appl. Mater. Interfaces XXXX, XXX, XXX−XXX

Notes

The authors declare no competing financial interest.

■ ACKNOWLEDGMENTS

This material is based upon work supported partially by the National Science Foundation under grant no. 2229155. The opinions, findings, and conclusions or recommendations expressed are those of the authors and do not necessarily reflect the views of the National Science Foundation.

■ REFERENCES

(1) He, M.; Yang, J.; Gu, M.; Wu, Y.; Chen, K.; Sun, Y.; Qi, D. Bioinspired interfacial engineering of multiscale micro/nano-structured surfaces with robust superhydrophobic and tunable adhesion. *Chem. Eng. J.* **2024**, *501*, 157482.

(2) Wijerathne, B.; Liao, T.; Jiang, X.; Zhou, J.; Sun, Z. Plant-inspired surfaces and interfaces for sustainable technologies. *Mater. Futures* **2025**, *4* (1), 012301.

(3) Wijerathne, B.; Liao, T.; Ostrikov, K.; Sun, Z. Bioinspired Robust Mechanical Properties for Advanced Materials. *Small Struct.* **2022**, *3* (9), 2100228.

(4) Mei, J.; Liao, T.; Peng, H.; Sun, Z. Bioinspired Materials for Energy Storage. *Small Methods* **2022**, *6* (2), 2101076.

(5) Barthlott, W.; Schimmel, T.; Wiersch, S.; Koch, K.; Brede, M.; Barczewski, M.; Walheim, S.; Weis, A.; Kaltenmaier, A.; Leder, A.; Bohn, H. F. The Salvinia Paradox: Superhydrophobic Surfaces with Hydrophilic Pins for Air Retention Under Water. *Adv. Mater.* **2010**, *22* (21), 2325−2328.

(6) Silvestre, M. L. T.; Zambrano, A. R. C.; Linis, V. C.; Janairo, J. I. B. Surface morphological and wetting characterization of the hydrophobic and superhydrophobic leaves of Pistia stratiotes L., Salvinia molesta D.Mitch., Ananas comosus (L.) Merr. and Dyckia platyphylla L.B. Smith for bioinspired oil adsorbent materials. *IOP Conf Ser. Mater. Sci. Eng.* **2019**, *479* (1), 012003.

(7) Zhang, D.; Ji, J.; Yan, C.; Zhang, J.; An, Z.; Shen, Y. Research advances in bio-inspired superhydrophobic surface: Bridging nature to practical applications. *J. Ind. Eng. Chem.* **2024**, *140*, 20−46.

(8) Speichermann-Jägel, L.; Dullenkopf-Beck, S.; Droll, R.; Gandyra, D.; Barczewski, M.; Walheim, S.; Schimmel, T. Stable Air Retention under Water on Artificial Salvinia Surfaces Enabled by the Air Spring Effect: The Importance of Geometrical and Surface-Energy Barriers, and of the Air Spring Height. *Adv. Mater. Interfaces* **2024**, *11* (36), 2400400.

(9) Huang, C.; Qian, L. Effect of groove sizes on the dynamic behavior of droplets impacting grooved cylindrical superhydrophobic surfaces. *Int. J. Multiphase Flow* **2025**, *185*, 105134.

(10) Tian, F.; Yu, R.; Zuo, X.; Zhang, M.; Zhao, L.; Zhao, X.; Yang, X.; Zhang, Y.; Huang, W. Bioinspired 3D printed elastomer-hydrogel hybrid with robust interfacial bonding for flexible ionotronics. *Chem. Eng. J.* **2024**, *489*, 151164.

(11) Sparks, S. S.; Obando, A. G.; Li, Y.; Chen, S.; Yao, S.; Qiu, K. 3D-printed biomimetic and bioinspired soft actuators. *IET Cyber-Syst. Robot.* **2024**, *6* (4), No. e70001.

(12) Xu, Y.; Mao, H.; Liu, C.; Du, Z.; Yan, W.; Yang, Z.; Partanen, J.; Chen, Y. Hopping Light Vat Photopolymerization for Multiscale Fabrication. *Small* **2023**, *19* (11), 2205784.

(13) Shi, Z.; Zhang, Z.; Huang, W.; Zeng, H.; Mandić, V.; Hu, X.; Zhao, L.; Zhang, X. Spontaneous Adsorption-Induced Salvinia-like Micropillars with High Adhesion. *Langmuir* **2021**, *37* (22), 6728−6735.

(14) Yang, Y.; Li, X.; Zheng, X.; Chen, Z.; Zhou, Q.; Chen, Y. 3D-Printed Biomimetic Super-Hydrophobic Structure for Microdroplet Manipulation and Oil/Water Separation. *Adv. Mater.* **2018**, *30* (9), 1704912.

(15) Sikulskyi, S.; Srinivasaraghavan Govindarajan, R.; Stark, T.; Ren, Z.; Reed, N.; Kim, D. Two-photon polymerized wetting morphologies for tunable external and internal electrode micro-patterning. *Addit. Manuf.* **2024**, *86*, 104220.

(16) Lantada, A. D.; Hengsbach, S.; Bade, K. Lotus-on-chip: computer-aided design and 3D direct laser writing of bioinspired surfaces for controlling the wettability of materials and devices. *Bioinspiration Biomimetics* **2017**, *12* (6), 066004.

(17) He, Q.; Tang, T.; Zeng, Y.; Iradukunda, N.; Bethers, B.; Li, X.; Yang, Y. Review on 3D Printing of Bioinspired Structures for Surface/Interface Applications. *Adv. Funct. Mater.* **2024**, *34* (11), 2309323.

(18) Ren, Z.; Yang, Z.; Srinivasaraghavan Govindarajan, R.; Madiyar, F.; Cheng, M.; Kim, D.; Jiang, Y. Two-Photon Polymerization of Butterfly Wing Scale Inspired Surfaces with Anisotropic Wettability. *ACS Appl. Mater. Interfaces* **2024**, *16* (7), 9362−9370.

(19) Jiang, L. J.; Campbell, J. H.; Lu, Y. F.; Bernat, T.; Petta, N. Direct Writing Target Structures by Two-Photon Polymerization. *Fusion Sci. Technol.* **2016**, *70* (2), 295−309.

(20) Jiang, L. J.; Maruo, S.; Osellame, R.; Xiong, W.; Campbell, J. H.; Lu, Y. F. Femtosecond laser direct writing in transparent materials based on nonlinear absorption. *MRS Bull.* **2016**, *41* (12), 975−983.

(21) Tricinci, O.; Terencio, T.; Mazzolai, B.; Pugno, N. M.; Greco, F.; Mattoli, V. 3D Micropatterned Surface Inspired by Salvinia molesta via Direct Laser Lithography. *ACS Appl. Mater. Interfaces* **2015**, *7* (46), 25560−25567.

(22) Tricinci, O.; Pignatelli, F.; Mattoli, V. 3D Micropatterned Functional Surface Inspired by Salvinia Molesta via Direct Laser Lithography for Air Retention and Drag Reduction. *Adv. Funct. Mater.* **2023**, *33* (39), 2206946.

(23) Sun, Y.; Guo, Z. Recent advances of bioinspired functional materials with specific wettability: from nature and beyond nature. *Nanoscale Horiz.* **2019**, *4* (1), 52−76.

(24) Chi, J.; Zhang, X.; Wang, Y.; Shao, C.; Shang, L.; Zhao, Y. Bio-inspired wettability patterns for biomedical applications. *Mater. Horiz.* **2021**, *8* (1), 124−144.

(25) Shi, Z.; Zeng, H.; Yuan, Y.; Shi, N.; Wen, L.; Rong, H.; Zhu, D.; Hu, L.; Ji, L.; Zhao, L.; Zhang, X.; et al. Constructing Super-hydrophobicity by Self-Assembly of SiO2@Polydopamine Core-Shell Nanospheres with Robust Oil-Water Separation Efficiency and Anti-Corrosion Performance. *Adv. Funct. Mater.* **2023**, *33* (16), 2213042.

(26) Zhu, D.; Liu, W.; Zhao, R.; Shi, Z.; Tan, X.; Zhang, Z.; Li, Y.; Ji, L.; Zhang, X. Microscopic insights into hydrophobicity of cerium oxide: Effects of crystal orientation and lattice constant. *J. Mater. Sci. Technol.* **2022**, *109*, 20−29.

(27) Zhu, D.; Hu, C.; Zhao, R.; Tan, X.; Li, Y.; Mandić, V.; Shi, Z.; Zhang, X. Fabrication of cerium oxide films with thickness and hydrophobicity gradients. *Surf. Coat. Technol.* **2022**, *430*, 127985.

(28) Zhu, D.; Tan, X.; Ji, L.; Shi, Z.; Zhang, X. Preparation of transparent and hydrophobic cerium oxide films with stable mechanical properties by magnetron sputtering. *Vacuum* **2021**, *184*, 109888.

(29) Sun, Y.; Wang, Y.; Sui, X.; Liang, W.; He, L.; Wang, F.; Yang, B. Biomimetic Multiwalled Carbon Nanotube/Polydimethylsiloxane Nanocomposites with Temperature-Controlled, Hydrophobic, and Icephobic Properties. *ACS Appl. Nano Mater.* **2021**, *4* (10), 10852−10863.

(30) Li, D.; Liang, X.; Li, S.; Wang, T.; Han, G.; Guo, Z. Bioinspired textile with dual-stimuli responsive wettability for body moisture management and signal expression. *New J. Chem.* **2021**, *45* (27), 12193−12202.

(31) Wu, Y.; Sun, R.; Ren, J.; Zhang, S.; Wu, S. Bioinspired Dynamic Camouflage in Programmable Thermochromic-Patterned Photonic Films for Sophisticated Anti-Counterfeiting. *Adv. Funct. Mater.* **2023**, *33* (7), 2210047.

(32) Yang, K.; Chen, S.; Liu, Y.; Liang, Y.; Zhang, Z.; Liu, C. Adhesion switchable transition on bio-inspired Janus surface for multi-directional droplet manipulation. *Chem. Eng. J* **2024**, *496*, 154254.

(33) Wei, C.; Zong, Y.; Jiang, Y. Bioinspired Wire-on-Pillar Magneto-Responsive Superhydrophobic Arrays. *ACS Appl. Mater. Interfaces* **2023**, *15* (20), 24989−24998.

https://doi.org/10.1021/acsami.5c10911
ACS Appl. Mater. Interfaces XXXX, XXX, XXX−XXX

(34) Wang, L.; Zhang, C.; Wei, Z.; Xin, Z. Bioinspired Fluoride-Free Magnetic Microcilia Arrays for Anti-Icing and Multidimensional Droplet Manipulation. *ACS Nano* **2024**, *18* (1), 526−538.
(35) Wang, J.; Gao, W.; Zhang, H.; Zou, M.; Chen, Y.; Zhao, Y. Programmable wettability on photocontrolled graphene film. *Sci. Adv.* **2018**, *4* (9), No. eaat7392.
(36) Yilmaz, M.; Kuloglu, H. B.; Erdogan, H.; Cetin, S. S.; Yavuz, M. S.; Ince, G. O.; Demirel, G. Light-driven unidirectional liquid motion on anisotropic gold nanorod arrays. *Adv. Mater. Interfaces* **2015**, *2* (12), 1500226.
(37) Shao, H.; Yin, K.; Xu, N.; Zhang, Y.; Shi, Z.; Zhou, Y.; Luo, Z.; Wang, D.; Deng, X. Adaptive Surfaces with Stimuli-Responsive Wettability: From Tailoring to Applications. *ACS Nano* **2025**, *19* (7), 6729−6747.
(38) Leverant, C. J.; Zhang, Y.; Cordoba, M. A.; Leo, S.-Y.; Charpota, N.; Taylor, C.; Jiang, P. Macroporous Superhydrophobic Coatings with Switchable Wettability Enabled by Smart Shape Memory Polymers. *Adv. Mater. Interfaces* **2021**, *8* (13), 2002111.
(39) Okada, K.; Miura, Y.; Chiya, T.; Tokudome, Y.; Takahashi, M. Thermo-responsive wettability via surface roughness change on polymer-coated titanate nanorod brushes toward fast and multi-directional droplet transport. *RSC Adv.* **2020**, *10* (47), 28032−28036.
(40) Zheng, J.; Yang, B.; Wang, H.; Zhou, L.; Zhang, Z.; Zhou, Z. Temperature-Responsive Femtosecond Laser-Ablated Ceramic Surfaces with Switchable Wettability for On-Demand Droplet Transfer. *ACS Appl. Mater. Interfaces* **2023**, *15* (10), 13740−13752.
(41) Zheng, L.; Li, H.; Huang, W.; Lai, X.; Zeng, X. Light Stimuli-Responsive Superhydrophobic Films for Electric Switches and Water-Droplet Manipulation. *ACS Appl. Mater. Interfaces* **2021**, *13* (30), 36621−36631.
(42) Park, S.; Bang, J.; So, H. 3D printing-assisted and magnetically-actuated superhydrophobic surfaces for droplet control. *Surf. Interfaces* **2023**, *37*, 102678.
(43) Hanosh, S.; Lekshmi, B. S.; Varanakkottu, S. N.; George, S. D. Simple Fabrication of PDMS-Grafted Hydrophobic Iron Oxide Particles for Oil−Water Separation and Stimuli-Responsive Liquid Marbles. *ACS Appl. Polym. Mater.* **2023**, *5* (5), 3507−3514.
(44) Chen, G.; Dai, Z.; Li, S.; Huang, Y.; Xu, Y.; She, J.; Zhou, B. Magnetically Responsive Film Decorated with Microcilia for Robust and Controllable Manipulation of Droplets. *ACS Appl. Mater. Interfaces* **2021**, *13* (1), 1754−1765.
(45) Su, Y.; Fan, X.; Zhu, S.; Li, Z.; Bian, Y.; Li, C.; Zhang, Y.; Liu, L.; Hu, Y.; Li, J.; Wu, D. Magnetism-Actuated Superhydrophobic Flexible Microclaw: From Spatial Microdroplet Maneuvering to Cross-Species Control. *ACS Appl. Mater. Interfaces* **2021**, *13* (29), 35165−35172.
(46) Jia, Z.; Chang, C.; Hu, S.; Li, J.; Ge, M.; Dong, W.; Ma, H. Artificial intelligence-enabled multipurpose smart detection in active-matrix electrowetting-on-dielectric digital microfluidics. *Microsyst. Nanoeng.* **2024**, *10* (1), 139.
(47) Tan, J.; Fan, Z.; Zhou, M.; Liu, T.; Sun, S.; Chen, G.; Song, Y.; Wang, Z.; Jiang, D. Orbital Electrowetting-on-Dielectric for Droplet Manipulation on Superhydrophobic Surfaces. *Adv. Mater.* **2024**, *36* (24), 2314346.
(48) Cao, J.; Zeng, X.; Shen, S.; Feng, H.; Qin, X.; Jin, M.; Liu, Z.; Yan, Z.; Shui, L. Replaceable Dielectric Film for Low-Voltage and High-Performance Electrowetting-Based Digital Microfluidics. *Langmuir* **2023**, *39* (29), 10189−10198.
(49) Li, Y.; Li, J.; Liu, L.; Yan, Y.; Zhang, Q.; Zhang, N.; He, L.; Liu, Y.; Zhang, X.; Tian, D.; et al. Switchable Wettability and Adhesion of Micro/Nanostructured Elastomer Surface via Electric Field for Dynamic Liquid Droplet Manipulation. *Adv. Sci.* **2020**, *7* (18), 2000772.
(50) Jun, K.; Kim, D.; Ryu, S.; Oh, I.-K. Surface Modification of Anisotropic Dielectric Elastomer Actuators with Uni- and Bi-axially Wrinkled Carbon Electrodes for Wettability Control. *Sci. Rep.* **2017**, *7* (1), 6091.
(51) Sikulskyi, S.; Ren, Z.; Mekonnen, D. T.; Holyoak, A.; Srinivasaraghavan Govindarajan, R.; Kim, D. Additively manufactured unimorph dielectric elastomer actuators: Design, materials, and fabrication. *Front. Rob. AI* **2022**, *9*, 1034914.
(52) Guo, Y.; Liu, L.; Liu, Y.; Leng, J. Review of Dielectric Elastomer Actuators and Their Applications in Soft Robots. *Adv. Intell. Syst.* **2021**, *3* (10), 2000282.
(53) Wang, H.; Yang, L.; Zhang, X.; Ang, M. H. Effect of different prestretching index and preloading on actuation behaviors of dielectric elastomer actuator. *J. Mater. Res. Technol.* **2021**, *15*, 4064−4073.
(54) Iannarelli, A.; Niasar, M. G.; Ross, R. The effects of static pre-stretching on the short and long-term reliability of dielectric elastomer actuators. *Smart Mater. Struct.* **2019**, *28* (12), 125014.
(55) Wiranata, A.; Ishii, Y.; Hosoya, N.; Maeda, S. Simple and Reliable Fabrication Method for Polydimethylsiloxane Dielectric Elastomer Actuators Using Carbon Nanotube Powder Electrodes. *Adv. Eng. Mater.* **2021**, *23* (6), 2001181.
(56) de Saint-Aubin, C. A.; Rosset, S.; Schlatter, S.; Shea, H. High-cycle electromechanical aging of dielectric elastomer actuators with carbon-based electrodes. *Smart Mater. Struct.* **2018**, *27* (7), 074002.
(57) Wang, D.; Wang, J.; Shen, Z.; Jiang, C.; Zou, J.; Dong, L.; Fang, N. X.; Gu, G. Soft Actuators and Robots Enabled by Additive Manufacturing. *Annu. Rev. Control Rob. Auton. Syst.* **2023**, *6*, 31−63.
(58) Guo, Z.; Yu, P.; Li, B.; Xuan, F.; Zhao, J. Direct wire writing technique benefitting the flexible electronics. *Virtual Phys. Prototyping* **2024**, *19* (1), No. e2286514.
(59) Mansour, S. A.; Elsad, R. A.; Izzularab, M. A. Dielectric properties enhancement of PVC nanodielectrics based on synthesized ZnO nanoparticles. *J. Polym. Res.* **2016**, *23* (5), 85.
(60) Shrestha, M.; Asundi, A.; Lau, G.-K. Smart Window Based on Electric Unfolding of Microwrinkled TiO2 Nanometric Films. *ACS Photonics* **2018**, *5* (8), 3255−3262.
(61) Li, Y.; Park, S.; McLamb, M.; Lata, M.; Schöche, S.; Childers, D.; Aggarwal, I. D.; Poutous, M. K.; Boreman, G.; Hofmann, T. UV to NIR optical properties of IP-Dip, IP-L, and IP-S after two-photon polymerization determined by spectroscopic ellipsometry. *Opt. Mater. Express* **2019**, *9* (11), 4318−4328.
(62) Feigl, G.; Zaugg, D.; Hinum-Wagner, J. W.; Hörmann, S. M.; Bergmann, A. Refractive index characterization and modeling of polymerization-dependent refractive index variations in two-photon polymerization resins. *Opt. Continuum* **2025**, *4* (5), 996−1005.

https://doi.org/10.1021/acsami.5c10911
ACS Appl. Mater. Interfaces XXXX, XXX, XXX−XXX